A comparison between holographic and near-field ptychographic X-ray tomography for solid oxide cell materials

F Monaco, M Hubert, Julio Cesar da Silva, V Favre-Nicolin, D Montinaro, P Cloetens, J Laurencin

A Comparison Between Holographic and Near-Field Ptychographic X-ray Tomography for Solid Oxide Cell Materials

F. Monaco[a,b*], M. Hubert[a], J.C. Da Silva[b,c], V. Favre-Nicolin[b], D. Montinaro[d], P. Cloetens[b], J. Laurencin[a]

[a]Univ. Grenoble Alpes – CEA/LITEN, 17 rue des Martyrs, 38054, Grenoble, France

[b] ESRF – The European Synchrotron, 71 Avenue des Martyrs, 38043 Grenoble, France

[c] Univ. Grenoble Alpes, CNRS, Grenoble INP, Institut Néel, 25 Avenue des Martyrs, 38042 Grenoble, France

[d] SOLIDpower S.p.A., 38017 Mezzolombardo, Italy

Abstract.

Holographic and near-field ptychographic X-ray computed tomography techniques have been compared by characterizing a typical solid oxide cell hydrogen electrode using a high-energy X-ray beam. The main advantages and drawbacks of both methods are discussed regarding the possibility to image the Ni-YSZ cermet, a complex porous electrode microstructure composed of X-ray absorbent materials. The same innovative sub-pixel alignment algorithm, based on tomographic consistency, was applied to align the different tomographic projections for each technique. It has been shown that a better signal-to-noise ratio (SNR) is obtained using near-field ptychographic tomography, whereas holographic tomography can be faster with similar spatial resolution. Moreover, quantitative electron density maps have been obtained with the two techniques. The quality of the phase identification has also been assessed and compared in both cases using a classical grey-level class separability criterion. After the segmentation, a set of typical microstructural properties describing the electrode morphology was computed. The comparison of the results allowed validating the complementarity of the two X-ray imaging techniques. Despite the more time-consuming data acquisition and processing than holographic tomography, near-field ptychographic tomography is especially well adapted to image samples without any insight on their composition or when the sample is highly absorbent. Yet, holographic X-ray tomography, using high-energy X-rays to reduce the sample absorption, remains a faster 3D imaging technique with spatial resolution and contrast sensitivity sufficient for the characterization of solid oxide cell materials.

Keywords: nano-tomography, X-ray holography, X-ray ptychography, Solid Oxide Fuel Cell, Solid Oxide Electrolysis Cell, microstructure, Ni-YSZ cermet

*Corresponding author: Telephone: + 33 4 76 88 23 26, E-mail: federico.monaco@esrf.fr

1 Introduction

In recent years, the need for volumetric material characterization at the nanoscale has grown significantly due to the increase of applications that require the knowledge of the structural properties at this length scale. Besides, large fields of view (FOV) are typically needed to extract statistically relevant properties from the 3D volumes. In this context, high-temperature Solid Oxide Cells (SOCs) are a representative example of a technology for which a deep knowledge of the microstructure is needed to understand the global behavior.

SOCs can be used as an efficient electrochemical converter operating either in Fuel Cell mode (SOFC) or Electrolysis mode (SOEC). Nevertheless, the SOCs performances and especially their durability must be further improved [Irvine2016, Udomsilp2020]. In particular, the electrodes suffer from chemical and morphological instabilities upon an operation that needs to be solved [Moçoteguy2013, Chen2016, Khan2016]. One of the main milestones is the improvement of the porous hydrogen electrode made of a cermet of Nickel and Yttria Stabilized Zirconia (Ni-YSZ). Indeed, this electrode is submitted to morphological evolutions of the metallic phase, due to Ni agglomeration and migration, contributing significantly to the global loss of cell performance [Faes2009, Hubert2018a, Monaco2019, Trini2020]. These phenomena are responsible for a substantial particle coarsening as well as a depletion of Ni at the electrolyte interface in electrolysis mode. Because of the complex microstructure of this porous composite, 2D observations are insufficient and 3D reconstructions are required. In this frame, a high spatial resolution of a few tens of nanometers is needed to image the morphological changes in the material [Joos2012, Hubert2016] whereas a large FOV is required to catch the different length-scale and heterogeneities of the microstructure.

The Representative Volume Element (RVE) is a keystone in the electrode microstructural analyses. The dimension of the RVE is dependent on the microstructure of the electrode as well as the examined microstructural properties [Harris2015]. For example, in [Moussaoui2018], the RVE of an H_2 electrode active layer with a fine microstructure has been evaluated at $15 \times 15 \times 15$ μm^3. This value is increased to a volume of $36 \times 36 \times 36$ μm^3 for a support layer with a coarse microstructure [Moussaoui2020]. When the characterization is focused on aged samples, it should be noticed that the RVE can be increased to obtain an accurate microstructural quantification [Jiao2016]. It is essential to combine a large field of view with a high spatial resolution. Indeed, small voxel sizes are required to well define particles and microstructural evolutions. In [Joos2012], it is considered that about ten voxels per particle diameter are the minimum required to describe correctly a material

phase. With this rule, the resolution should be at least around 75 nm to well describe a Ni-YSZ microstructure of a typical H_2 electrode [Joos2012].

To fulfill all these requirements for the reconstruction of the SOCs electrodes, several characterization techniques can be used. The first method for the 3D electrode imaging is based on a Scanning Electron Microscope (SEM) combined with a Focused Ion Beam (FIB) working with Gallium ions [Wilson2006, Kanno2011, Holzer2011, Joos2014, Matsui2010, Prokop2018, Vivet2011]. This so-called FIB-SEM tomography technique presents the advantage of the high 2D resolution of the SEM images. However, the reconstructed volume size could be limited due to the rather long milling process. To overcome this issue, a new equipment using plasma-FIB working with Xenon ions (PFIB) has been developed to reach higher currents for the milling. It allows increasing the size of the analyzed volume, which is especially well adapted to observe the potential heterogeneities in the electrode microstructure [Mahbub2017, Mahbub2020]. Even if the thickness direction is still limited in size [Mahbub2020], volumes as large as $130 \times 189 \times 11.5\ \mu m^3$ have been obtained with this recent technique with a reported isotropic resolution of 65 nm.

Another category of techniques for 3D characterization of materials is the X-ray computed tomography methods. In this domain, the feasibility to reconstruct a Ni-YSZ cermet using a laboratory equipment has been recently reported in [Heenan2017, Heenan2018]. In these studies, the authors have been able to distinguish the porosity network and the two solid phases of the electrode. Nevertheless, despite the convenience of this technique, the sample must be restricted to a relatively small size to have enough transmission at the low available X-ray energy. Besides, the photon flux is quite limited, implying long scans and exposure times with potential drifts of the sample. To go faster in the data acquisition, the use of synchrotron X-ray radiation with higher photon flux is required. Several works have been dedicated to the 3D electrode reconstruction using synchrotron tomography. Some of them have taken advantage of the Ni absorption K-edge at 8.33 keV [Shearing2010, Guan2011, Chen-Wiegart2012], recording the data below and above this threshold to obtain Ni-specific contrast in the projections. Another recent solution is far-field Ptychographic X-ray Computed Tomography (PXCT) [Dierolf2010], which has recently provided relevant results on the Ni-YSZ cermet [DeAngelis2018, DeAngelis2020]. Despite the two solid phases can be clearly separated in the reconstructions, both techniques are performed at low beam energy, limiting the sample size due to the strongly absorbent materials of SOC. In parallel, Holographic X-ray Computed Tomography (HXCT) [Cloetens1999] using high-energy X-rays, mostly above 30 keV, has been applied to the characterization of SOCs materials [Laurencin2012, Villanova2013, Hubert2016]. The

main advantage of high-energy HXCT is that the sample size can be increased to diameters of more than 50 µm without compromising the X-ray transmission.

Regarding their advantages and drawbacks, although FIB-SEM provides the best spatial resolution, even if often anisotropic, the synchrotron X-ray-based methods are liable to reach highly resolved volumes [Hubert2018b, DeAngelis2017]. Moreover, X-ray tomography is not destructive and the microstructural evolution such as Ni coarsening can be imaged on the same sample [Shearing2012, Chen-Wiegart2016, DeAngelis2017]. Therefore, the FIB-SEM and X-ray tomographic approaches are complementary material characterization techniques with a partial overlap in terms of accessible reconstructed volume size and spatial resolution [Williams2011]. In this frame, several publications have been devoted to compare the two techniques for cross-validation. In [Nelson2011], a comparison is proposed between FIB-SEM and synchrotron X-ray nanotomography working around the Mn K-edge of an O_2 composite electrode. The microstructural properties extracted from both volumes are confronted and a generally good agreement is found in the analyses. In [Quey2013], the results of HXCT applied to the characterization of the Ni-YSZ sample are compared with SEM images obtained on the same sample to validate the HXCT approach. After an image registration procedure, the images were compared to check the accuracy of the microstructure reconstruction by holotomography showing a good agreement in the calculated properties and thus confirming the validity of the holotomographic reconstruction.

Despite their recent advancement and validations, the X-ray tomographic methods must be further improved to reach the large number of requirements necessary for a precise characterization of the electrode microstructure. On the one hand, progress is underway in combining multiscale characterization techniques. For example, the global porosity of a specific H_2 electrode has been imaged in [Lu2017] with a micro-tomographic equipment while geometrical details have been resolved using nanoscale characterizations. On the other hand, a new promising technique named Near-Field Ptychography (NFP) has been developed in recent years [Stockmar2013]. Combined with computed tomography, Near-Field Ptychographic X-ray Computed Tomography (NF-PXCT) enables high-resolution and high-sensitivity imaging of larger field-of-view relative to the ones obtained by HXCT or by far-field PXCT.

We have previously published a first proof-of-feasibility of the use of this technique for the characterization of SOC materials [Stockmar2015]. In the present work, a direct comparison between HXCT and NF-PXCT on the same sample is presented. To do so, the acquisition and reconstruction

time for each technique are considered. To allow a proper comparison, all the experiments have been performed on the same sample and using the same instrument, which was the beamline ID16A of the European Synchrotron Radiation Facility (ESRF). Before the tomographic reconstruction, the tomographic projections were aligned using the same innovative sub-pixel registration algorithm based on tomographic consistency conditions. Although common for NF-PXCT, this was the first time those algorithms were successfully applied to HXCT data. In addition, the electron density maps are extracted from the two reconstructions and the quantitative values obtained for each phase are compared with the expected ones. Moreover, the quality of the obtained gray-level 3D reconstructions is analyzed in terms of spatial resolution and signal-to-noise ratio (SNR). Finally, the microstructural properties of the 3D inner microstructure of SOC materials obtained from both techniques are compared and the relevance of the two tomographic methods for this type of application is discussed.

2 Materials and Methods

2.1 Cell Description and Sample Preparation

A state of the art hydrogen electrode supported cell was provided by SOLIDpower SPA to be used for this work. The characterization has been focused on the interface between the electrolyte and the H_2 electrode. The electrolyte is a dense layer made of 8% Yttria Stabilized Zirconia (8YSZ). The electrode consists of a ceramic-metallic composite of Nickel and YSZ (Ni-YSZ cermet). The Ni and YSZ phases are expected to represent proportions of about 40%vol and 60%vol in the solid phase of the H_2 electrode according to the manufacturer. Before the characterization, the cell has been aged for 15000 hours in fuel cell mode. The durability test specifications are detailed in [Monaco2019].

A sample has been extracted from the outlet of the aged cell for the tomographic experiments. The specimen has been prepared by using a Plasma Focused Ion Beam (PFIB Vion FEI^{TM}). This equipment allows the choice of the location of the sample as well as the control of the final geometry. In our case, the cylindrical geometry is well adapted to the tomography procedure around a vertical axis. Moreover, this equipment is using Xenon ions for milling the material. This technology is faster than conventional Ga^+ FIB since higher currents can be reached [Burnett2016]. The detailed procedure for sample milling and extraction can be found in [Hubert2016]. The pillar mounted directly on a pin adapted for the tomographic experiments is cut to the final diameter at low current. In this way, the surface is clean and the sample geometry meets the requirements for the beamline

experiment. The final sample is shown in Figure 1, in which the region of interest (ROI) containing the Ni-YSZ cermet in the vicinity of the electrolyte is highlighted.

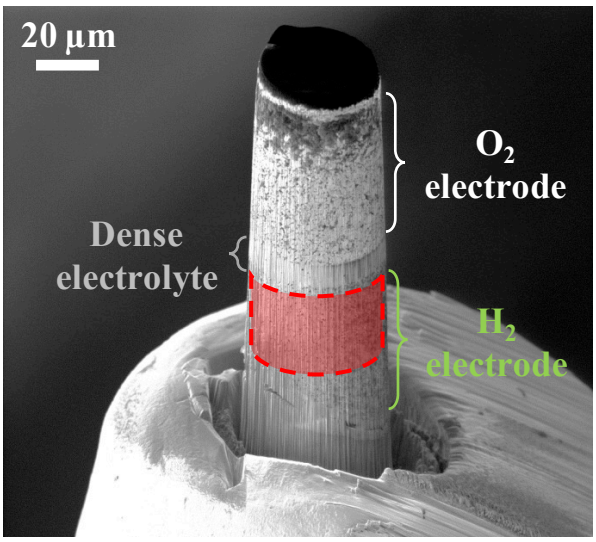

Figure 1 – Sample prepared by PFIB for the tomographic experiments (the ROI in the sample is highlighted in red).

2.2 3D-Characterization Techniques

The data acquisitions have been performed on the Nano-Imaging ID16A beamline at the European Synchrotron Radiation Facility (ESRF) [DaSilva2017a, Villar2018]. This beamline has been designed for hard X-ray imaging techniques reaching a high spatial resolution. Two discrete energies at 17 keV and 33.6 keV are available for experiments. To obtain a highly coherent beam, the distance between the source and the sample has been set to 185 meters. As illustrated in Figure 2, multilayer-coated Kirkpatrick-Baez (KB) mirrors are used to focus the X-ray beam into a circular spot of about 12 nm in diameter [DaSilva2017b]. Two pairs of mirrors have been specifically designed to cover the two energies of the beamline. After the focal point, the beam is divergent with a well-defined cone geometry (Figure 2). The sample is positioned between the focal point and the detector with a small range piezo-driven hexapod specifically developed at the ESRF for the beamline to reach the required nano-positioning and stability [Villar2018]. To maintain the stability of the experimental station during the scans, the high-precision translation motors move at slow speeds of 4µm/s and 1µm/s, for horizontal and vertical directions, respectively. All the KB nano-focusing optics and the sample stage are located in a large vessel under vacuum.

Both NF-PXCT and HXCT use a similar experimental setup. The projections are recorded on a FReLoN CCD based detector [Labiche2007] with 4096 × 4096 pixels and an effective pixel size of 1.5 µm, which were binned by a factor 2 achieving an array of 2048 × 2048 pixels and a pixel size of

3 µm. The focus and detector positions have been fixed during the acquisitions, allowing the selection of a target pixel size in the projections by taking advantage of the magnification and choosing the position of the sample along the beam axis. Due to a technical issue with the sample stage, for this experiment the rotation axis could not be aligned orthogonally to the incoming X-ray beam. To compensate for the residual tilt of 13.17 mrad, a cone-beam tomographic reconstruction algorithm was used, in which we supposed the sample was at the corner of the cone-beam. For these cone-beam calculations, the source to sample distance was set equal to the focus to sample position (0.01 m) and we calculated the pixel position on the detector in which the beam is normal to the detector surface (p_{det_normal}) as follow:

$$p_{det\_normal} = p_{img\_center} + \alpha \frac{Z_{12}}{ps_{detector}} \quad (1)$$

where p_{img_center} is the pixel at the center of the image along the vertical direction, $ps_{detector}$ is the detector pixel size, Z_{12} is the focus-to-detector position, and α is the angle of the residual tilt. For both HXCT and NF-PXCT, Z_{12}= 1.2648 m, $ps_{detector}$ = 3 µm, and the p_{img_center} was set to different values for each technique, because the image sizes are different, but their values are given below when describing the acquisition and data analysis of the two techniques.

The high energy of 33.6 keV is especially well adapted for holographic imaging of strongly absorbent materials like the ceramics in the SOC electrodes, although it would not have been needed for NF-PXCT as the latter handle better X-ray absorbent sample even at lower energies. The specificities of the two characterization techniques are detailed hereafter.

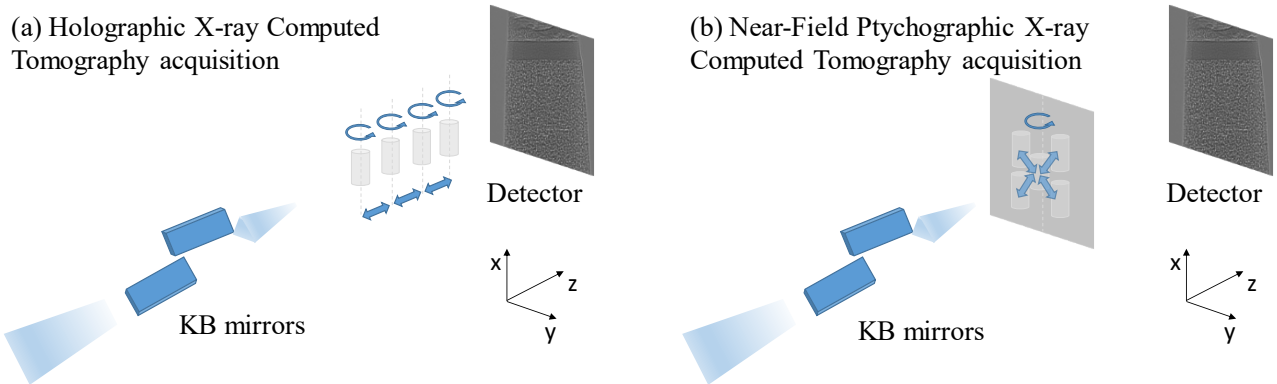

Figure 2 – Schematic representation for the tomographic acquisition on the ID16A beamline: (a) Holographic X-ray Computed Tomography (HXCT), in which a tomographic experiment is repeated at each of the four different positions along the z-axis. (b) Near-Field Ptychographic X-ray Computed Tomography (NF-PXCT), in which a tomographic experiment is repeated at each of the different lateral positions in the xy-plane (four acquisitions are taken around each one of the four positions given in the graph, in addition to the projection taken in the center, resulting in a total of 17 positions).

Holographic X-ray Computed Tomography (HXCT) – HXCT is a full-field imaging technique combining X-ray inline holography and computed tomography, which takes advantage of the geometric magnification effect of a divergent cone beam to achieve a given voxel size in the final reconstruction [Mokso2007]. It consists of the acquisition of holograms over 180° at four different sample positions along the optical axis as shown in Figure 2a. The longitudinal diversity allows enhancing the final resolution in the volume thanks to the increase of information [Mokso2007]. The first distance gives the highest magnification and it is chosen to set the voxel size equal to 25 nm in this experiment. This value is a good compromise to reach a high resolution while keeping a large field of view. A total of 1500 projections have been recorded over 180° for each distance of the HXCT scan with an exposure time of 0.5 seconds. This number of projections sets the maximum achievable resolution to 42 nm for a sample pillar of 40µm-diameter according to Crowther's criterion [Crowther1970]. A specific procedure of adding a random lateral motion of the sample at each angle has been used to avoid ring-shape artifacts in the reconstructions [Hubert2018b]. Projections without the sample as well as dark images have also been recorded at each distance to perform a flat-field correction for each projection. Subsequently, the projections of the 2nd, 3rd, and 4th distances are resized via interpolation to match the pixel size of the 1st distance.

After flat-field correction, the resized projections at the four distances are accurately aligned to each other. Afterwards, an iterative holographic phase retrieval procedure adapted for strongly absorbent materials, such as SOCs, has been used to obtain a phase map for each angle [Villanova2013]. The method is initiated using the Paganin approach [Paganin2002] and assuming the chemical composition of the cermet and well-dispersed phases, resulting in a relatively homogeneous sample. Thanks to this assumption, the ratio between the refractive index decrement δ and the absorption coefficient β can be estimated ($\delta/\beta \approx 58$). This estimation is used as first guess in an iterative nonlinear Conjugate Gradient Method (CGM) that allows converging to a satisfactory solution for the phase map at each angle. Before the tomographic reconstruction, the phase maps have been aligned with subpixel precision using the open-source software Toupy [https://doi.org/10.5281/zenodo.3515942] and following an approach based on tomographic consistency [Guizar-Sicairos2011, Guizar-Sicairos2015]. Despite being common for NF-PXCT, this was the first time this sub-pixel alignment was successfully applied to HXCT and it proved to be superior to the standard phase-correlation-based alignment algorithms. The final tomographic reconstruction step is performed by using the filtered back-projection (FBP) algorithm for cone-beam geometry on the aligned phase maps using PyHST2 [Mirone2014]. For this specific reconstruction, p_{img_center}= 1024 and p_{det_normal} = 6577. In this experiment, a cylinder of $51.2 \times \pi \times 25.6^2$ =105360 µm^3 has been reconstructed and the

obtained volume is a 3D map of the refractive index decrement δ, which is proportional to the electron density of the materials present in the sample.

Near-Field Ptychographic X-ray Computed Tomography (NF-PXCT) – This method is also a full-field technique, but differently from HXCT, the holograms are recorded at different lateral sample positions with a coherent and structured beam at each angle [Stockmar2013]. Figure 2b displays a schematic representation of the experimental setup. The projections are magnified by the cone-beam geometry, allowing the choice of the voxel size in the reconstruction. As for the HXCT reconstruction, the distance has been selected in order to obtain a voxel size of 25 nm in the final 3D volume in this case. One of the main advantages of NF-PXCT relative to HXCT is related to the fact that with this technique no insights on the sample, such as its composition, are required for the reconstruction. In addition, with NF-PXCT it is possible to reconstruct satisfactorily well strongly absorbent objects even at lower X-ray energies [Stockmar2013, Stockmar2015], although this feature will not be relevant for this comparison with HXCT since the two experiments were performed at 33.6 keV. Moreover, the probe and the object are both retrieved, which allows accounting correctly for heterogeneities present in the incoming beam. Experimentally, for each of the 1200 angles regularly distributed over an angular range of 180°, 17 pseudo-randomly distributed projections have been recorded. According to Crowther's criterion [Crowther1970], this number of projections sets the maximum achievable resolution to about 52 nm for a sample pillar of 40μm-diameter [Crowther1970]. An exposure time of 0.5 seconds has been used for each projection. Moreover, projections without the sample as well as dark images have been recorded at the beginning and at the end of the acquisition, even if, in principle, the flat-field images are not necessary for NF-PXCT.

The phase retrieval is performed by using two Python packages: Ptypy [Enders2016] was used for data preparation and first phase retrieval trials; PyNX [Favre-Nicolin2020] was then used to optimize the reconstruction parameters to leverage convergence issues due to the large phase gradient [Stockmar2015b], and to accelerate the calculation of the relatively big volume of data. The phase retrieval was performed using the Difference Map (DM) algorithm [Thibault2009], combined with the Alternating Projections (AP) and the Maximum Likelihood (ML) algorithms [Thibault2012]. The first projection was optimized using 23000 cycles of DM algorithm, 4000 of AP and 1000 conjugate gradient ML. The following projections used the previous one as a starting point with 1500 DM, 2000 AP and 500 ML cycles. Similar to HXCT, the tomographic reconstruction is performed on the aligned phase maps using a classical FBP algorithm for cone-beam geometry, implemented in PyHST2 [Mirone2014], leading to a cylindrical 3D reconstruction with a slightly larger volume than the one

obtained by HXCT ($58.7 \times \pi \times 29.9^2 = 164866$ µm^3). For this particular reconstruction, p_{img_center}= 1196 and p_{det_normal} = 6726.47.

2.3 Image Processing and Microstructural Properties Computation

The two reconstructed 3D images have been processed using in-house developed scripts for segmentation and computation of the microstructural properties following the procedure that is described hereafter. Firstly, the same cubic sub-volumes have been cropped from the ROI, located in the vicinity of the interface between the electrode and the electrolyte. This was done to analyze comparable reconstructions in the electrode functional layer of $\approx 28 \times 28 \times 28$ µm^3, much larger than the RVE of this electrode, estimated to be around 15^3 µm^3 [Moussaoui2018]. Then, the data have been processed with an anisotropic diffusion filter to enhance the grey-level separation between porosity, YSZ and Ni [Perona1990]. Afterward, the filtered 3D reconstructions have been segmented univocally labeling each one of the material phases by using Otsu's technique [Otsu1979]. Subsequently, the segmented volumes have been analyzed with in-house algorithms that are described in detail in [Moussaoui2018, Laurencin2012]. Briefly, after the identification and the labeling of the connected domains for each phase (Ni, pores and YSZ), the corresponding volume fractions of each phase have been determined (Vf_{Ni}, Vf_{pores} and Vf_{YSZ}). Moreover, the specific surface areas between the different phases ($Sp_{Ni\text{-}pores}$, $Sp_{YSZ\text{-}pores}$, $Sp_{Ni\text{-}YSZ}$) have been extracted, as well as the mean phase diameter ($\overline{D}_{Ni}$, $\overline{D}_{pores}$ and $\overline{D}_{YSZ}$), and the tortuosity factor (τ_{Ni}, τ_{pores} and τ_{YSZ}) for each phase. Finally, the density of Triple Phase Boundary lengths (TPBls) (defined as the lines where the pore, Ni and YSZ meet in the microstructure), which represent the active sites for the electrochemical reactions, has been calculated.

3 Results and Discussion

3.1 Comparison of Acquisition and Reconstruction Times

The first aspect that can be analyzed to compare the HXCT and NF-PXCT techniques is the duration of the data acquisition. For holotomography, the parameters used for the experiment resulted in a tomographic scan time of about 5 hours. In comparison, the NF-PXCT scan took about 19 hours to record all projections for the sample. This longer duration for NF-PXCT can be explained by two main aspects: the larger number of images acquired (17 *vs* 4 images per projection angle) and the relatively slow motion of the motors at the ID16A beamline. The latter factor dominates the overall

scan duration for this type of large ROI reconstructed. In fact, to assure the stability of the sample during the movement, the displacement of the sample in the xy-plane was carried out by piezo motors with low speed (4 x 1 μm/s (H x V)) at the time of the experiment [Villar2018]. Consequently, the acquisition overhead is 84%, i.e., excluding the exposure time (17×0.5 s = 8.5 s), the remaining 84% of the scan duration is spent to move the motors. Therefore, the acquisition time is strongly impacted by the experimental setup of the beamline and may change for other beamlines using, for example, faster motors and an interferometric system to correct for instabilities of the motors during the acquisition [Holler2014, Engblom2019].

The second point of comparison between the two techniques is the duration of the procedure for the phase retrieval followed by the tomographic reconstruction. For the HXCT, the assumption on the sample δ/β ratio and the utilization of Paganin's method to provide a first estimate of the phase map, guarantees a low number of iterations of the non-linear CGM to reach convergence. Indeed, only 15 iterations [Hubert2017] are needed to retrieve the phase map with a small error leading to a computing time of about 8 hours (using parallelization of the calculations on 72 CPU cores of the ESRF computing cluster corresponding to 576 CPU-hours). For the NF-PXCT algorithm, instead, more iterations and a longer computing time are needed. This can be associated with the larger number of images per projection angle and with the coupled retrieval of the phase and the amplitude for both the illumination (probe) and the sample (object). Because of the large number of iterations of the NF-PXCT phase retrieval algorithm, this procedure is computationally intensive and requires access to highly performant clusters to combine the 17 projections at each angle and retrieve one phase map. For this reason, the reconstruction was done using the IDRIS Ouessant GPU cluster. Moreover, the 1200 projections were divided into 30 NVidia P100 GPU, each one optimizing independently a group of 40 angles. The computation time was 7.5 hours, corresponding to 223 GPU-hours.

From this discussion, it appears that the NF-PXCT requires more intensive computation due to the larger volume of data treated, the coupled retrieval of probe and object, and to the absence of prior hypotheses on the sample composition. This adds to the larger acquisition time needed to scan the same ROI. Note however that the long computation time for NF-PXCT is mostly due to the large phase gradient for the thick object [Stockmar2015b] compared to the surrounding vacuum. Convergence for thin objects (phase shift $< \pi$, e.g. for local tomography) would require between one and two orders of magnitude fewer calculations, between 1 to a few minutes per projection angle for the ptychography reconstruction. Whereas the larger acquisition time is mostly due to the overhead of 84% of the scan motors of ID16A beamline.

3.2 Electron Density Maps

From the 3D phase maps obtained via HXCT and NF-PXCT it is possible to obtain the local electron density in the sample, which is directly proportional to the refractive index decrement δ. Indeed, the grey-levels (ω) in the volumes correspond to $-2\pi/\lambda \cdot \delta$ where λ is the wavelength of the photons. Based on this definition and considering an offset selected to have the air outside the sample corresponding to zero [Weber2016], the refractive index decrement can be directly determined. Subsequently, for each voxel in the sample the corresponding electron density is obtained using Equation (2) [Diaz2012].

$$n_e = \frac{2\pi}{\lambda^2 r_e}\delta \tag{2}$$

In which n_e is the electron density (Å^{-3}) and r_e is the classical electron radius. Here we assume a X-ray energy far from any absorption edge of the elements present in the sample. Figure 3 shows a comparison between 2D slices extracted from the electron density maps obtained with the two techniques.

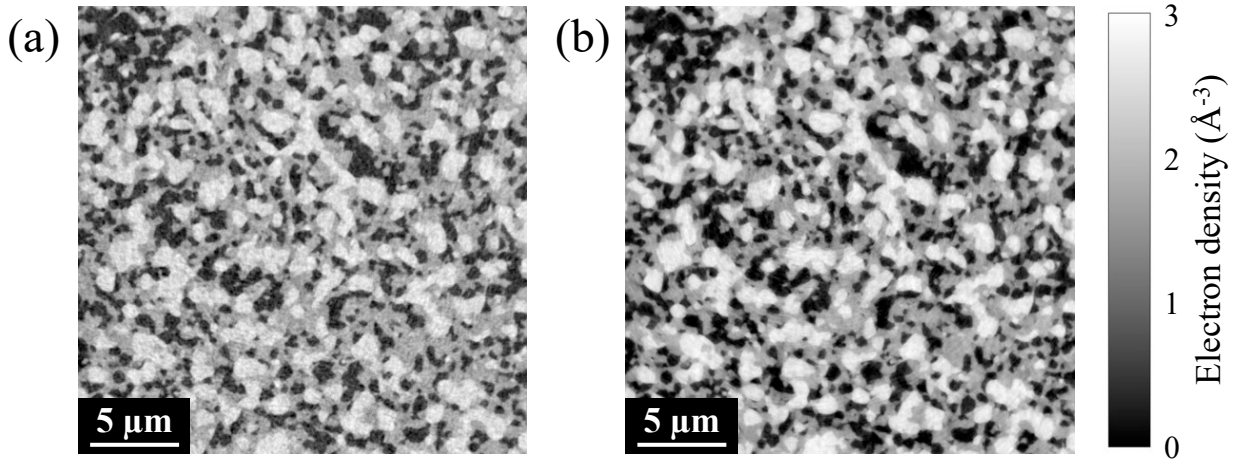

Figure 3 – 2D slices of electron density maps obtained with the two techniques: (a) Holographic X-ray Computed Tomography (HXCT). (b) Near-Field Ptychographic X-ray Computed Tomography (NF-PXCT).

A specific procedure reported in the supplementary materials (S1) has been used to obtain the local electron density for each solid phase in the sample and the values have been compared with the expected ones. The results are shown in Figure S2 of the supplementary materials and in Table I, in which it can be clearly seen that both techniques allow obtaining a good estimation of the material density for the Ni and the YSZ with an error < 10%. Based on the experimental conditions in which the sample was tested [Monaco2019], it is expected that the Ni should be present in the metallic form. Nevertheless, from the HXCT and the NF-PXCT data, we cannot rule out completely the presence of

a mixture of Ni and NiO, as the value obtained for the electron density of the Ni phase is in between the two. This indicates that some particles of Nickel oxide could be present in the sample. In this case, the transformation oxidation of Ni might be only superficial and might have been induced by the sample preparation with PFIB and/or by the exposition of a certain X-ray radiation dose follow to exposure to air.

Table I – Comparison between the expected electron density of the different solid phases and the values obtained by HXCT and NF-PXCT following the procedure reported in the supplementary material (the values in parentheses represent the standard deviations).

	Ni	**YSZ**	**NiO**
HXCT	2.31 (0.20)	1.62 (0.20)	-
NF-PXCT	2.30 (0.16)	1.49 (0.17)	-
Expected	2.56	1.64	1.94

3.3 Reconstruction Data Quality

The visual inspection of the 2D slices taken from the electron density maps obtained with the HXCT and NF-PXCT reconstructions (Figure 3a and 3b) reveals that the NF-PXCT image is less noisy than the HXCT one. This is also confirmed by the smaller standard deviation obtained when calculating the electron density of each solid phase (cf. Table I). To quantify more precisely the quality of the images, the Signal-to-Noise Ratio (SNR) has been measured on the grey-level volumes obtained by HXCT and NF-PXCT. This ratio provides an insight into the proportion of the background noise in the relevant signal for the 3D image. Among the existing definitions [Welvaert2013, Vanpeene2020], the simple expression given in Equation (3), has been used for the SNR:

$$SNR = \mu_{YSZ}/\sigma_{bkg} \tag{3}$$

Where μ_{YSZ} is the mean grey-level value measured for the YSZ phase and $\sigma_{bkg}$is the standard deviation of the background measured in a region selected outside the sample (in the air/vacuum). It has been found that the SNR increases from 16 for the HXCT dataset to 39 for the NF-PXCT reconstruction. This quantification clearly confirms the lower noise in the reconstruction obtained with NF-PXCT. The enhancement in the quality of the volume was expected with the NF-PXCT algorithm as with this technique the probe is reconstructed in parallel to the object which offers the possibility to consider rigorously the incident beam heterogeneities in the phase map retrieval. This correction is partially taken into account using a flat-field procedure for the HXCT projections. However, this procedure is only an approximation as discussed in [Hubert2018b]. The random motion

approach blurs artifacts related to this approximation, but an increased noise level cannot be avoided with a finite number of projections.

To go further in the analysis, another crucial parameter is the spatial resolution of the 3D image. To estimate this value, several techniques can be used [Holler2014]. A simple solution is to plot the grey-level edge profile across the interface between two material phases. By fitting this profile with a hyperbolic tangent function and by considering a 10%-90% criterion, it is possible to estimate the spatial resolution. This technique requires detecting the normal direction to the blurred interface. As this step is a source of uncertainty, the measurement has to be repeated several times for better statistics. An illustration of this measurement is reported in the supplementary materials (S2). By using this approach, a spatial resolution of 52.5 nm has been measured in the HXCT volume. This result, about two pixels, is in good agreement with a previous evaluation made on SOC electrode material [Hubert2018b]. For the NF-PXCT reconstruction, using the same approach, the spatial resolution has been estimated at 58.5 nm. Both estimated resolution values are in a reasonably good agreement with the expected value of 42 nm and 52 nm for HXCT and NF-PXCT, respectively, calculated based on the Crowther's criterion. This indicates that both techniques yield 3D images with practically the same spatial resolution. Finally, it can be noticed that the spatial resolutions obtained in both cases are sufficient to satisfactorily describe all the geometrical characteristics in the H_2 electrode according to the criteria proposed in the literature [Joos2012, Harris2015].

3.4 Segmentation Quality

The segmentation, consisting of attributing each grey-level voxel to one of the electrode phases (Ni, YSZ or porosity), is a crucial step in the full procedure for the microstructural properties' extraction. The ideal case for a perfect segmentation would be a histogram with well-separated grey-level peaks corresponding to each electrode phase. Nevertheless, the grey-level distributions between phases are most of the time overlapping for real samples. To circumvent this issue and to improve the peak separation in the histogram, the raw data have been preprocessed applying an anisotropic diffusion filter [Perona1990, Villanova2013] as discussed in Section 2.3. Before the segmentation, the HXCT volume has been additionally processed with a median filter with a window size of 3 × 3. This supplementary step is required for this dataset due to the higher noise in the image. The improvement in the histogram separability achieved thanks to the filtering is shown in Figure 4 in which it can be clearly seen that the separation between the peaks corresponding to each phase is successfully improved.

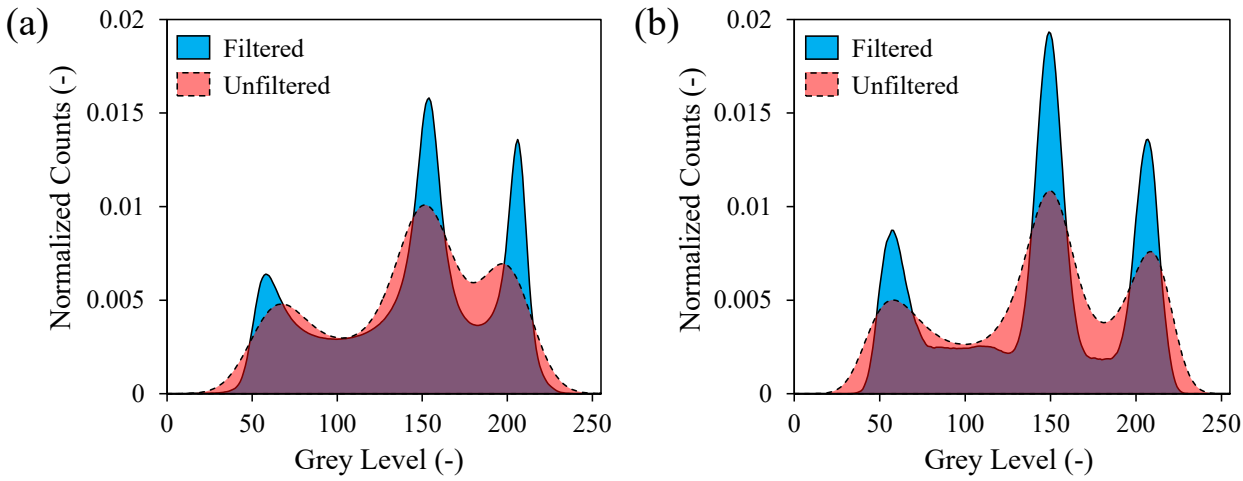

Figure 4 – 8bit grey-level histograms before and after filtering for the two reconstruction techniques: (a) HXCT and (b) NF-PXCT.

Subsequently, the segmentation between porosities, YSZ and Ni has been performed by using Otsu's method. In this segmentation method, the optimal segmentation is identified by maximizing the between-class variance of the different grey-level phases [Otsu1979]. One of the advantages of Otsu's method is the possibility to compute a criterion that indicates the quality of the data segmentation. This criterion is obtained by calculating the ratio of the between-class variance and the total variance in the volume. A value equal to one indicates a perfect segmentation (Dirac distribution of grey-levels), whereas a low value reveals a high uncertainty in the electrode phase labeling. Computation of Otsu's criterion has been done on all grey-leveled data. Without filtering, this indicator decreases from 0.899 for the NF-PXCT volume to 0.884 for the HXCT volume. This result reveals a better grey-level separation in the NF-PXCT dataset that can be directly linked with the higher SNR obtained for this volume. Therefore, the signal for each phase is better defined in the histogram, whereas the noise in the HXCT increases the overlap between peaks. The Otsu's criterion has also been measured after the histogram enhancement with the filters. In this case, the criterion is substantially increased for both reconstructions to reach 0.932 for the NF-PXCT and 0.906 for the HXCT. Even after the application of the additional median filter to the HXCT dataset, the phases separability criterion remains higher for the NF-PXCT volume due to the larger separation between the peaks obtained using this technique. Nevertheless, the quality of the segmentation has been clearly improved for both reconstructions by the image filtering.

3D renderings and a 2D cross-section for each segmented volume are shown in Figure 5. At a first visual inspection, the reconstructions obtained with the two techniques are quite similar. This is confirmed by the identification of the three phases for both techniques shown in the 2D cross-sections. However, the renderings of isolated Ni particles indicate a noticeable difference: the particles are

smaller and more numerous according to HXCT as compared to NF-PXCT. This observation could be an artifact originated from a slightly less precise segmentation associated to the higher noise, with salt-and-pepper aspect, in the HXCT dataset. Nevertheless, for both techniques the fraction of isolated particles remains very limited (1% for HXCT *vs* 1.5% for NF-PXCT).

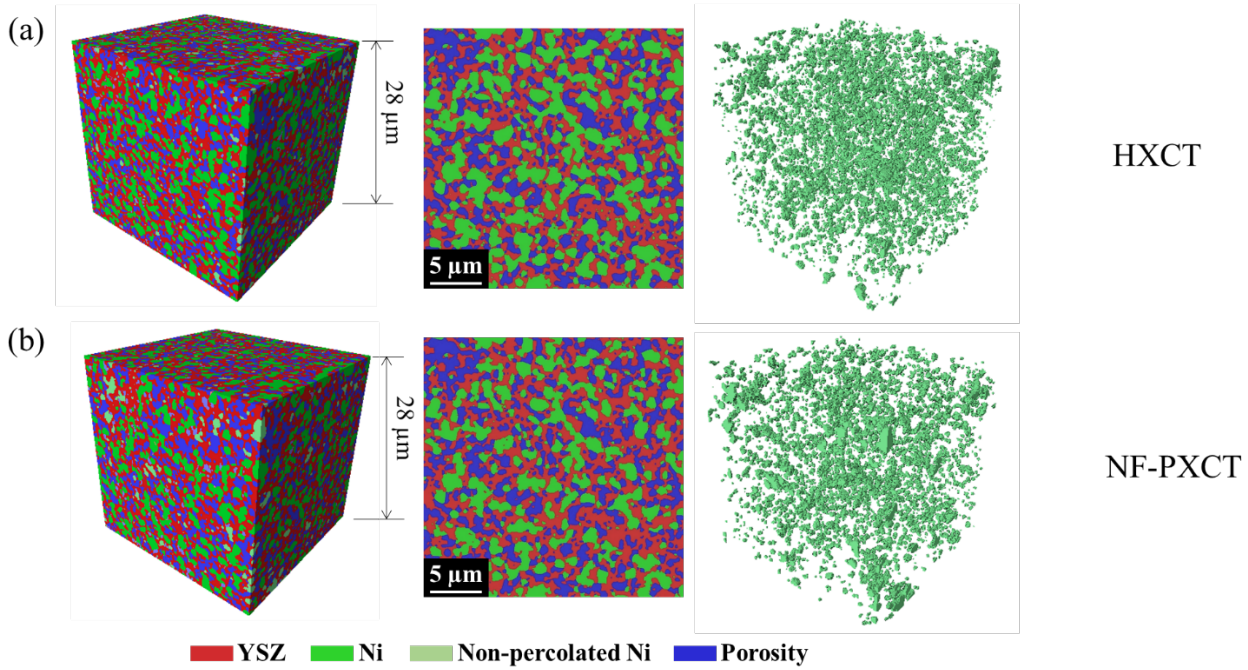

Figure 5 – 3D renderings, 2D cross-sections and isolated nickel particles extracted from the reconstructions obtained with the two techniques: (a) HXCT and (b) NF-PXCT.

To finalize the comparison, the relevant microstructural parameters of the electrode have been extracted from the two volumes and have been compared between each other.

3.5 Microstructural Properties

The microstructural properties have been computed on the same cubic sub-volumes located at the interface between the electrode and the electrolyte. The results for both reconstructions are shown in Table II for comparison. It should be noticed that the parameters have been computed on the connected materials corresponding to the electrochemically active phases. All the parameters are in excellent agreement for both volumes. The volume fractions for Ni and YSZ in the solid phase (41%Ni–59%YSZ and 39%Ni–61%YSZ for HXCT and NF-PXCT, respectively) are in perfect agreement with the manufacturer specifications. For all the other microstructural properties, the difference between the values obtained with HXCT and NF-PXCT does not exceed 6% except for the tortuosity factor of the Nickel phase. For this parameter, the difference between the two techniques is about 17%. This difference could be explained by the slightly higher proportion of disconnected Ni in the NF-PXCT reconstruction (cf. Figure 5 and Table II). Overall, it can be seen that both

techniques allow obtaining similar results in terms of microstructural parameters and can be used to characterize absorbent materials with complex microstructure like SOC hydrogen electrodes.

Table II – Microstructural parameters obtained from the HXCT and NF-PXCT techniques.

	HXCT	**NF-PXCT**	**%diff.**
Percolation pores (-)	0.979	0.982	0.31%
Percolation YSZ (-)	1.00	1.00	0.00%
Percolation Ni (-)	0.960	0.943	1.77%
Volume fraction pores (-)	0.278	0.277	0.36%
Volume fraction YSZ (-)	0.419	0.426	1.67%
Volume fraction Ni (-)	0.288	0.278	3.47%
Sp pores/YSZ ($\mu m^2/\mu m^3$)	1.7564	1.8595	5.87%
Sp pores/Ni ($\mu m^2/\mu m^3$)	0.3754	0.3981	6.05%
Sp Ni/YSZ ($\mu m^2/\mu m^3$)	1.2261	1.2012	2.03%
Tortuosity factor pores (-)	7.0210	7.2553	3.34%
Tortuosity factor YSZ (-)	2.1714	2.1567	0.68%
Tortuosity factor Ni (-)	8.4035	9.8376	17.07%
TPBl ($\mu m/\mu m^3$)	3.602	3.754	4.22%
Mean diameter pores (μm)	0.48	0.45	6.25%
Mean diameter YSZ (μm)	0.42	0.41	2.38%
Mean diameter Ni (μm)	0.70	0.68	2.86%

4 Conclusion

The same Ni-YSZ electrode has been characterized by synchrotron HXCT and NF-PXCT techniques. The procedures to obtain the 3D volumes, the reconstruction quality and the extracted microstructural parameters have been compared to discuss the advantages and drawbacks of each technique. Considering the acquisition and reconstruction duration, it appears that NF-PXCT is much more time-consuming when the region of interest is large. This is due to the large number of transversal images required for the reconstruction and the relatively slow transverse motion of ID16A beamline motors. With faster translation motors, this overhead can be substantially reduced. Moreover, a large number of images at each angle requires intensive computation for the retrieval of probes and objects. These two drawbacks of NF-PXCT could be improved in the future by taking advantage of the redundancies in the tomographic acquisition to reduce the number of recorded images per angle. Moreover, the electron density maps have been extracted from the two volumes and a good quantitative agreement between the expected values and the calculated ones has been found for both techniques.

Besides, the quality of the reconstructed volumes has been compared through different indicators. The SNR clearly revealed that the NF-PXCT provides less noisy 3D data. However, the spatial resolution measurement evaluated by the edge profile method has not revealed an improvement with NF-PXCT, which clearly indicated the SNR and spatial resolution are two independent factors. These results illustrate that NF-PXCT is especially efficient to decrease the noise in the 3D volume. Thus, this technique is particularly well adapted when noise can be detrimental to accurately distinguish phases with similar densities. In our case, the HXCT volume is additionally filtered with a median filter to remove this noise before segmentation. Comparing the feasibility of phase identification, the NF-PXCT histogram presents a better separation of the peaks. Otherwise, the segmentation of the complex hydrogen electrode microstructure is satisfactory for both techniques.

The microstructural properties extracted from the 3D reconstructions have been compared between HXCT and NF-PXCT. The results have shown an excellent agreement between the two characterization techniques. This result allows validating the perfect consistency of NF-PXCT for SOC materials confirming that this technique is suitable for the characterization of strongly absorbent materials with high quality. Therefore, NF-PXCT can be especially relevant for microstructures with multiple phases requiring low noise images or when the sample composition is unclear, as no insights on the chemical composition of the materials are necessary in this case.

Acknowledgments

The authors acknowledge access to the nano-characterization platform (PFNC) at the Minatec Campus in Grenoble. The HXCT and NF-PXCT experiments were performed at the beamline ID16A at the European Synchrotron Radiation Facility (ESRF), Grenoble, France, in the frame of proposal MA-3495. This work was granted access to the HPC resources of IDRIS under the allocation 2018-AP011010655 made by GENCI.

References

[Burnett2016] Burnett, T. L., Kelley, R., Winiarski, B., Contreras, L., Daly, M., Gholinia, A., Burke, M. G., Withers, P. J. (2016). Large volume serial section tomography by Xe Plasma FIB dual beam microscopy. Ultramicroscopy, 161, 119-129.

[Chen2016] Chen, K. (2016). Materials degradation of solid oxide electrolysis cells. Journal of The Electrochemical Society, 163(11), F3070.

[Chen-Wiegart2012] Chen-Wiegart, Y. C. K., Cronin, J. S., Yuan, Q., Yakal-Kremski, K. J., Barnett, S. A., & Wang, J. (2012). 3D Non-destructive morphological analysis of a solid oxide fuel cell anode using full-field X-ray nano-tomography. Journal of Power Sources, 218, 348-351.

[Chen-Wiegart2016] Chen-Wiegart, Y. C. K., Kennouche, D., Scott Cronin, J., Barnett, S. A., & Wang, J. (2016). Effect of Ni content on the morphological evolution of Ni-YSZ solid oxide fuel cell electrodes. Applied Physics Letters, 108(8), 083903.

[Cloetens1999] Cloetens, P., Ludwig, W., Baruchel, J., Van Dyck, D., Van Landuyt, J., Guigay, J. P., & Schlenker, M. (1999). Holotomography: Quantitative phase tomography with micrometer resolution using hard synchrotron radiation x rays. Applied Physics Letters, 75(19), 2912.

[DaSilva2017a] Da Silva, J. C., Haubrich, J., Requena, G., Hubert, M., Pacureanu, A., Bloch, L., Yang, Y., & Cloetens, P. (2017). High energy near- and far-field ptychographic tomography at the ESRF. Proceedings of SPIE, 10391, 1039106-1.

[DaSilva2017b] Da Silva, J. C., Pacureanu, A., Yang, Y., Bohic, S., Morawe, C., Barrett, R., & Cloetens, P. (2017). Efficient concentration of high-energy x-rays for diffraction-limited imaging resolution. Optica, 4(5), 492-495.

[Crowther1970] Crowther, R. A., DeRosier, D. J., & Klug, A. (1970). The reconstruction of a three-dimensional structure from projections and its application to electron microscopy, Proc. R. Soc. London A 317, 319.

[DeAngelis2017] De Angelis, S., Jørgensen, P. S., Esposito, V., Tsai, E. H. R., Holler, M., Kreka, K., & Bowen, J. R. (2017). Ex-situ tracking solid oxide cell electrode microstructural evolution in a redox cycle by high resolution ptychographic nanotomography. Journal of Power Sources, 360, 520-527.

[DeAngelis2018] De Angelis, S., Jørgensen, P. S., Tsai, E. H. R., Holler, M., Kreka, K., & Bowen, J. R. (2018). Three dimensional characterization of nickel coarsening in solid oxide cells via ex-situ ptychographic nano-tomography. Journal of Power Sources, 383, 72-79.

[DeAngelis2020] De Angelis, S., Jørgensen, P. S., Tsai, E. H. R., Holler, M., Fevola, G., & Bowen, J. R. (2020). Tracking nickel oxide reduction in solid oxide cells via ex-situ ptychographic nano-tomography. Materials Characterization, 162, 110183.

[Diaz2012] Diaz, A., Trtik, P., Guizar-Sicairos, M., Menzel, A., Thibault, P., & Bunk, O. (2012). Quantitative x-ray phase nanotomography. Physical Review B, 85, 020104.

[Dierolf2010] Dierolf, M., Menzel, A., Thibault, P., Schneider, P., Kewish, C. M., Wepf, R., Bunk, O., & Pfeiffer, F. (2010). Ptychographic X-ray computed tomography at the nanoscale. Nature, 467, 436.

[Enders2016] Enders, B., & Thibault, P. (2016). A computational framework for ptychographic reconstructions. Proceedings of the Royal Society A: Mathematical, Physical and Engineering Sciences, 472(2196), 20160640.

[Engblom2019] Engblom, C., Abiven, Y.-M., Alves, F., Berenguer, F., Bizien, T., Gibert, A., Langlois, F., Lestrade, A., Montaville, P., & Pérez, J.. (2019). 2D-Nano-ptychography imaging results on the SWING beamline at Synchrotron SOLEIL. Proceedings of 17th Int. Conf. on Acc. And Large Exp. Physics Control System (ICALEPCS2019), New York, NY, USA, pp. 91-96.

[Faes2009] Faes, A., Hessler-Wyser, A., Presvytes, D., Vayenas, C. G., & Van Herle, J. (2009). Nickel–zirconia anode degradation and triple phase boundary quantification from microstructural analysis. Fuel cells, 9(6), 841-851.

[Favre-Nicolin2020] Favre-Nicolin, V., Girard, G., Leake, S., Carnis, J., Chushkin, Y., Kieffer, J., Paleo, P., & Richard, M. I. (2020). PyNX: high-performance computing toolkit for coherent X-ray imaging based on operators. Journal of Applied Crystallography, 53, 1404-1413.

[Guan2011] Guan, Y., Gong, Y., Li, W., Gelb, J., Zhang, L., Liu, G., & Wang, H. (2011). Quantitative analysis of micro structural and conductivity evolution of Ni-YSZ anodes during thermal cycling based on nano-computed tomography. Journal of Power Sources, 196(24), 10601-10605.

[Guizar-Sicairos2011] Guizar-Sicairos, M., Diaz, A., Holler, M., Lucas, M. S., Menzel, A., Wepf, R. A., & Bunk, O. (2011). Phase tomography from x-ray coherent diffractive imaging projections. Optics Express, 19(22), 21345.

[Guizar-Sicairos2015] Guizar-Sicairos, M., Boon, J. J., Mader, K., Diaz, A., Menzel, A. & Bunk, O. (2015). Quantitative interior x-ray nanotomography by a hybrid imaging technique. Optica, 2(3), 259.

[Harris2015] Harris, W. M., & Chiu, W. K. (2015). Determining the representative volume element size for three-dimensional microstructural material characterization. Part 1: Predictive models. Journal of Power Sources, 282, 552-561.

[Heenan2017] Heenan, T. M., Bailey, J. J., Lu, X., Robinson, J. B., Iacoviello, F., Finegan, D. P., & Shearing, P. R. (2017). Three-phase segmentation of solid oxide fuel cell anode materials using lab based X-ray nano-computed tomography. Fuel Cells, 17(1), 75-82.

[Heenan2018] Heenan, T. M. M., Finegan, D. P., Tjaden, B., Lu, X., Iacoviello, F., Millichamp, J., & Shearing, P. R. (2018). 4D nano-tomography of electrochemical energy devices using lab-based X-ray imaging. Nano energy, 47, 556-565.

[Holler2014] Holler, M., Díaz, A., Guizar-Sicairos, M., Karvinen, P., Färm, E., Härkönen, E., & Bunk, O. (2014). X-ray ptychographic computed tomography at 16 nm isotropic 3D resolution. Scientific reports, 4(1), 1-5.

[Holzer2011] Holzer, L., Münch, B., Iwanschitz, B., Cantoni, M., Hocker, T., & Graule, T. (2011). Quantitative relationships between composition, particle size, triple phase boundary length and surface area in nickel-cermet anodes for Solid Oxide Fuel Cells. Journal of Power Sources, 196(17), 7076-7089.

[Hubert2016] M. Hubert, J. Laurencin, P. Cloetens, J.C. da Silva, F. Lefebvre-Joud, P. Bleuet, A. Nakajo, E. Siebert, Role of microstructure on electrode operating mechanisms for mixed ionic electronic conductors: From synchrotron-based 3D reconstruction to electrochemical modeling, Solid State Ionics. 294 (2016) 90–107.

[Hubert2017] M. Hubert, Durability of solid oxide cells: an experimental and modelling investigation based on synchrotron X-ray nano-tomography characterization, Thesis of Grenoble University, 2017

[Hubert2018a] Hubert, M., Laurencin, J., Cloetens, P., Morel, B., Montinaro, D., & Lefebvre-Joud, F. (2018). Impact of Nickel agglomeration on Solid Oxide Cell operated in fuel cell and electrolysis modes. Journal of Power Sources, 397, 240-251.

[Hubert2018b] Hubert, M., Pacureanu, A., Guilloud, C., Yang, Y., da Silva, J. C., Laurencin, J., & Cloetens, P. (2018). Efficient correction of wavefront inhomogeneities in X-ray holographic nanotomography by random sample displacement. Applied Physics Letters, 112(20), 203704.

[Irvine2016] Irvine, J. T., Neagu, D., Verbraeken, M. C., Chatzichristodoulou, C., Graves, C., & Mogensen, M. B. (2016). Evolution of the electrochemical interface in high-temperature fuel cells and electrolysers. Nature Energy, 1(1), 15014.

[Jiao2016] Jiao, Z., & Shikazono, N. (2016). 3D reconstruction size effect on the quantification of solid oxide fuel cell nickel–yttria-stabilized-zirconia anode microstructural information using scanning electron microscopy-focused ion beam technique. Science bulletin, 61(17), 1317-1323.

[Joos2012] Joos, J., Ender, M., Carraro, T., Weber, A., & Ivers-Tiffée, E. (2012). Representative volume element size for accurate solid oxide fuel cell cathode reconstructions from focused ion beam tomography data. Electrochimica Acta, 82, 268-276.

[Joos2014] Joos, J., Ender, M., Rotscholl, I., Menzler, N. H., & Ivers-Tiffée, E. (2014). Quantification of double-layer Ni/YSZ fuel cell anodes from focused ion beam tomography data. Journal of power sources, 246, 819-830.

[Kanno2011] Kanno, D., Shikazono, N., Takagi, N., Matsuzaki, K., & Kasagi, N. (2011). Evaluation of SOFC anode polarization simulation using three-dimensional microstructures reconstructed by FIB tomography. Electrochimica Acta, 56(11), 4015-4021.

[Khan2016] Khan, M. S., Lee, S. B., Song, R. H., Lee, J. W., Lim, T. H., & Park, S. J. (2016). Fundamental mechanisms involved in the degradation of nickel–yttria stabilized zirconia (Ni–YSZ) anode during solid oxide fuel cells operation: a review. Ceramics International, 42(1), 35-48.

[Labiche2007] Labiche, J. C., Mathon, O., Pascarelli, S., Newton, M. A., Ferre, G. G., Curfs, C., & Carreiras, D. F. (2007). Invited article: The fast readout low noise camera as a versatile x-ray detector for time resolved dispersive extended x-ray absorption fine structure and diffraction studies of dynamic problems in materials science, chemistry, and catalysis. Review of scientific instruments, 78(9), 091301.

[Laurencin2012] Laurencin, J., Quey, R., Delette, G., Suhonen, H., Cloetens, P., & Bleuet, P. (2012). Characterisation of Solid Oxide Fuel Cell Ni–8YSZ substrate by synchrotron X-ray nano-tomography: from 3D reconstruction to microstructure quantification. Journal of Power Sources, 198, 182-189.

[Lu2017] Lu, X., Li, T., Taiwo, O. O., Bailey, J., Heenan, T., Li, K., Brett, D. J. L., & Shearing, P. R. (2017). Study of the tortuosity factors at multi-scale for a novel-structured SOFC anode. X-ray Microscopy Conference, 849, 012020.

[Mahbub2017] Mahbub, R., Hsu, T., Epting, W. K., Nuhfer, N. T., Hackett, G. A., Abernathy, H., & Salvador, P. A. (2017). A method for quantitative 3D mesoscale analysis of solid oxide fuel cell microstructures using Xe-plasma focused ion beam (PFIB) coupled with SEM. ECS Transactions, 78(1), 2159.

[Mahbub2020] Mahbub, R., Epting, W. K., Hsu, T., Mason, J. H., Feng, M., Nuhfer, N. T., & Salvador, P. A. (2019). Quantitative Analysis of Multi-Scale Heterogeneities in Complex Electrode Microstructures. Journal of The Electrochemical Society, 167(5), 054506.

[Matsui2010] Matsui, T., Kishida, R., Kim, J. Y., Muroyama, H., & Eguchi, K. (2010). Performance deterioration of Ni–YSZ anode induced by electrochemically generated steam in solid oxide fuel cells. Journal of The Electrochemical Society, 157(5), B776-B781.

[Mirone2014] Mirone, A., Brun, E., Gouillart, E., Tafforeau, P., & Kieffer, J. (2014). The PyHST2 hybrid distributed code for high speed tomographic reconstruction with iterative reconstruction and a priori knowledge capabilities. Nuclear Instruments and Methods in Physics Research B, 324, 41-48.

[Moçoteguy2013] Moçoteguy, P., & Brisse, A. (2013). A review and comprehensive analysis of degradation mechanisms of solid oxide electrolysis cells. International journal of hydrogen energy, 38(36), 15887-15902.

[Mokso2007] Mokso, R., Cloetens, P., Maire, E., Ludwig, W., & Buffière, J. Y. (2007). Nanoscale zoom tomography with hard x rays using Kirkpatrick-Baez optics. Applied physics letters, 90(14), 144104.

[Monaco2019] F. Monaco, M. Hubert, J. Vulliet, J.P. Ouweltjes, D. Montinaro, P. Cloetens, P. Piccardo, F. Lefebvre-Joud, J. Laurencin, Degradation of Ni-YSZ Electrodes in Solid Oxide Cells: Impact of Polarization and Initial Microstructure on the Ni Evolution, J. Electrochem. Soc. 166 (2019) F1229–F1242.

[Moussaoui2018] Moussaoui, H., Laurencin, J., Gavet, Y., Delette, G., Hubert, M., Cloetens, P., & Debayle, J. (2018). Stochastic geometrical modeling of solid oxide cells electrodes validated on 3D reconstructions. Computational Materials Science, 143, 262-276.

[Moussaoui2020] Moussaoui, H., Debayle, J., Gavet, Y., Cloetens, P., & Laurencin, J. (2020). Particle-based model for functional and diffusion layers of solid oxide cells electrodes. Powder Technology, 367, 67-81.

[Nelson2011] Nelson, G. J., Harris, W.M., Lombardo, J. J., Izzo, J. R. Jr., Chiu, W. K. S., Tanasini, P., Cantoni, C., Van Herle, J., Comninellis, C., Andrews, J. C., Liu, Y., Pianetta, P., & Chu Y. S. (2011). Comparison of SOFC cathode microstructure quantified using X-ray nanotomography and focused ion beam–scanning electron microscopy. Electrochemistry Communications, 13, 586-589.

[Otsu1979] Otsu, N. (1979). A threshold selection method from gray-level histograms. IEEE transactions on systems, man, and cybernetics, 9(1), 62-66.

[Paganin2002] Paganin, D., Mayo, S. C., Gureyev, T. E., Miller P. R., & Wilkins, S. W. (2002). Simultaneous phase and amplitude extraction from a single defocused image of a homogeneous object. Journal of Microscopy, 206(1), 33-40.

[Perona1990] Perona, P., & Malik, J. (1990). Scale-space and edge detection using anisotropic diffusion. IEEE Transactions on pattern analysis and machine intelligence, 12(7), 629-639.

[Prokop2018] Prokop, T. A., Berent, K., Iwai, H., Szmyd, J. S., & Brus, G. (2018). A three-dimensional heterogeneity analysis of electrochemical energy conversion in SOFC anodes using electron nanotomography and mathematical modeling. International Journal of Hydrogen Energy, 43(21), 10016-10030.

[Quey2013] Quey, R., Suhonen, H., Laurencin, J., Cloetens, P., Bleuet, P. (2013). Direct comparison between X-ray nanotomography and scanning electron microscopy for the microstructure characterization of a solid oxide fuel cell anode. Material Characterization, 78, 87-95.

[Shearing2010] Shearing, P. R., Gelb, J., Yi, J., Lee, W. K., Drakopolous, M., & Brandon, N. P. (2010). Analysis of triple phase contact in Ni–YSZ microstructures using non-destructive X-ray tomography with synchrotron radiation. Electrochemistry Communications, 12(8), 1021-1024.

[Shearing2012] Shearing, P. R., Bradley, R. S., Gelb, J., Tariq, F., Withers, P. J., & Brandon, N. P. (2012). Exploring microstructural changes associated with oxidation in Ni–YSZ SOFC electrodes using high resolution X-ray computed tomography. Solid State Ionics, 216, 69-72.

[Stockmar2013] Stockmar, M., Cloetens, P., Zanette, I., Enders, B., Dierolf, M., Pfeiffer, F., & Thibault, P. (2013). Near-field ptychography: phase retrieval for inline holography using a structured illumination. Scientific reports, 3, 1927.

[Stockmar2015] Stockmar, M., Hubert, M., Dierolf, M., Enders, B., Clare, R., Allner, S., & Cloetens, P. (2015). X-ray nanotomography using near-field ptychography. Optics Express, 23(10), 12720-12731.

[Stockmar2015b] Stockmar, M., Zanette, I., Dierolf, M., Enders, B., Clare, R., Pfeiffer, F., Cloetens, P., Bonnin, A., & Thibault, P. (2015). X-Ray Near-Field Ptychography for Optically Thick Specimens. PHYSICAL REVIEW APPLIED, 3, 014005.

[Thibault2009] Thibault, P., Dierolf, M., Bunk, O., Menzel, A., & Pfeiffer, F. (2009). Probe retrieval in ptychographic coherent diffractive imaging. Ultramicroscopy, 109(4), 338-343.

[Thibault2012] Thibault, P., & Guizar-Sicairos, M. (2012). Maximum-likelihood refinement for coherent diffractive imaging. New Journal of Physics, 14(6), 063004.

[Trini2020] Trini, M., Hauch, A., De Angelis, S., Tong, X., Hendriksen, P. V., & Chen, M. (2020). Comparison of microstructural evolution of fuel electrodes in solid oxide fuel cells and electrolysis cells. Journal of Power Sources, 450, 227599.

[Udomsilp2020] Udomsilp, D., Rechberger, J., Neubauer, R., Bischof, C., Thaler, F., Schafbauer, W., & Guillon, O. (2020). Metal-Supported Solid Oxide Fuel Cells with Exceptionally High Power Density for Range Extender Systems. Cell Reports Physical Science, 100072.

[Vanpeene2020] Vanpeene, V., Villanova, J., Suuronen, J. P., King, A., Bonnin, A., Adrien, J., Maire, E. & Roué, L. (2020). Monitoring the morphological changes of Si-based electrodes by X-ray computed tomography: A 4D-multiscale approach. Nano Energy, 74, 104848.

[Villanova2013] Villanova, J., Laurencin, J., Cloetens, P., Bleuet, P., Delette, G., Suhonen, H., & Usseglio-Viretta, F. (2013). 3D phase mapping of solid oxide fuel cell YSZ/Ni cermet at the nanoscale by holographic X-ray nanotomography. Journal of Power Sources, 243, 841-849.

[Villar2018] Villar, F., Andre, L., Baker, R., Bohic, S., da Silva, J. C., Guilloud, C., & Salome, M. (2018). Nanopositioning for the ESRF ID16a nano-imaging beamline. Synchrotron Radiation News, 31(5), 9-14.

[Vivet2011] Vivet, N., Chupin, S., Estrade, E., Richard, A., Bonnamy, S., Rochais, D., & Bruneton, E. (2011). Effect of Ni content in SOFC Ni-YSZ cermets: A three-dimensional study by FIB-SEM tomography. Journal of Power Sources, 196(23), 9989-9997.

[Weber2016] Weber, L., Langer, M., Tavella, S., Ruggiu, A., & Peyrin, F. (2016). Quantitative evaluation of regularized phase retrieval algorithms on bone scaffolds seeded with bone cells. Physics in Medicine and Biology, 61, N215-N231.

[Welvaert2013] Welvaert, M., & Rosseel, Y. (2013). On the definition of signal-to-noise ratio and contrast-to-noise ratio for fMRI data. PloS one, 8(11).

[Williams2011] Williams, J. J., Chapman, N. C., Jakkali, V., Tanna, V. A., Chawla, N., Xiao, X., & De Carlo, F. (2011). Characterization of damage evolution in SiC particle reinforced Al alloy matrix composites by in-situ X-ray synchrotron tomography. Metallurgical and Materials Transactions A, 42(10), 2999-3005.

[Wilson2006] Wilson, J. R., Kobsiriphat, W., Mendoza, R., Chen, H. Y., Hiller, J. M., Miller, D. J., & Barnett, S. A. (2006). Three-dimensional reconstruction of a solid-oxide fuel-cell anode. Nature materials, 5(7), 541-544.